Electrochimica Acta 479 (2024) 143858

Contents lists available at ScienceDirect

Electrochimica Acta

journal homepage: www.journals.elsevier.com/electrochimica-acta

Enhanced lanthanum-stabilized low crystallinity metal oxide electrocatalysts with superior activity for oxygen reactions

M. García-Rodríguez [a], D. Cazorla-Amorós [b], E. Morallón [a,*]

[a] Departamento de Química Física e Instituto Universitario de Materiales, Universidad de Alicante, Ap. 99, E-03080, Alicante, Spain
[b] Departamento de Química Inorgánica e Instituto Universitario de Materiales, Universidad de Alicante, Ap. 99, E-03080, Alicante, Spain

ARTICLE INFO

Keywords:
Bifunctional electrocatalyst
Lanthanum
Metal oxides
Rechargeable Zn-air battery

ABSTRACT

Oxygen reduction reaction (ORR) and oxygen evolution reaction (OER) are key electrochemical reactions for the development of rechargeable Zn-air batteries. However, due to the high cost of commercial noble metal-based catalysts and their limited bifunctionality, it is necessary the design of new electrocatalysts. In this study, stable electrocatalysts have been synthesized through a hydrothermal method and further low-temperature thermal treatment. The materials consist of La stabilized low crystallinity Mn and Co metal (hydro-)oxides. The electrocatalytic performance of these materials has been compared with counterparts calcined at higher temperatures. The findings demonstrate that materials synthesized at lower temperatures and with low crystallinity exhibit superior electrocatalytic activity for both ORR and OER. Moreover, the research highlights the favorable influence of the lanthanum cation, which enhances changes of surface morphology and oxidation states of other cations (Mn and Co). Additionally, the positive contribution of the carbon component to electrochemical activity and electrical conductivity has been elucidated. The best electrocatalyst was studied in a rechargeable Zn-air battery with a durability of up to 120 h. They exhibited better stability and performance than the commercial Pt/C + RuO_2 catalyst currently used.

1. Introduction

Increasing energy demands have led to extensive research on high-efficiency, low-cost, and environmentally friendly alternative energy conversion and storage technologies [1,2]. Electrocatalysts for the oxygen reduction reaction (ORR) and oxygen evolution reaction (OER) are the cornerstone of future green energy applications because they participate in critical applications of renewable energy technologies such as fuel cells and metal-air batteries [3,4]. Despite significant efforts, producing bifunctional electrocatalysts for these two reactions remains a major challenge. The current limitation of fuel cells is the sluggish kinetics of ORR on the cathode side, while bifunctional ORR/OER catalysts are required for metal-air batteries [5]. Moreover, in polymer-electrolyte fuel cells (PEFCs), electrocatalysts represent almost 40 to 50 % of the overall cost of the fuel cell stack for automotive applications. Furthermore, a strategic analysis presented in the report by the US Fuel Cell Technologies Office (FCTO), predicts that the cost of the catalyst will be the largest for a single component of the PEFC stack, that is, 41% for 500,000 automotive systems per year [6,7]. Similarly to this, the cost and performance of Zn-air batteries are the most important technical issues for the target markets [8].

Noble metal-based materials are the best ORR and OER electrocatalysts, but due to their high cost, scarcity, and ineffective bifunctionality to these reactions, their implementation is impractical. Then, researchers are looking for more effective, extremely stable, and low-cost non-noble metal-based electrocatalysts [9] based on earth-abundant transition metal (hydro)oxides [10,11] and perovskite-type materials [12], among others. Some metals are active for the reactions of interest, such as Mn, Co, Ni…[13], and other metals do not exhibit electrocatalytic activity but provide stability to the structure and contribute to improve the electrocatalytic activity, i. e., lanthanum in perovskite-type metal oxides [14]. However, a major drawback of metal (hydro-)oxides is their poor electrical conductivity, which impedes the fast kinetics of electron transfer processes that are essential for driving electrochemical reactions. Carbon materials are often used to increase the electrical conductivity and the surface area of the electrocatalysts [15]. They also improve the transfer, diffusion and adsorption of oxygen and intermediate products on the electrocatalyst surface, which leads to improving the electrocatalytic activity [16–18].

On the other hand, the synthesis method is another important aspect

---

* Corresponding author.
E-mail address: morallon@ua.es (E. Morallón).

https://doi.org/10.1016/j.electacta.2024.143858
Received 7 October 2023; Received in revised form 16 January 2024; Accepted 19 January 2024

to consider. The right selection of the electrocatalyst preparation method is crucial for achieving sustainable production, both from economic and environmental points of view. Then, parameters like temperature, the nature of the precursors, the processing time, etc. must be considered. Recently, hydrothermal and solvothermal methods, which are environmentally friendly treatments, have been proposed as alternative synthesis methods of metal oxides [19].

In this work, we propose an environmentally friendly and low-cost hydrothermal synthesis method of metal oxides. This approach has been extremely successful in synthesizing nanomaterials of diverse shapes and sizes with low processing temperatures. Only water is used as solvent in a hydrothermal reaction procedure, which is performed in steel vessels (autoclaves) at temperatures between 100 and 200 °C to achieve water vapor saturation pressure [20,21]. This process provides a wide range of possibilities for tuning the morphological, optical, and structural properties of the materials by varying several experimental parameters or conditions [22]. One of them is the addition of a surfactant, which will modify the crystal growth kinetics [23], thus adjusting their shape and avoiding particle aggregation. Therefore, through this procedure, materials can be synthesized at low temperatures, taking advantage of the hydrothermal effect, and avoiding the use of polluting or expensive solvents.

In this study, we present the hydrothermal synthesis of metal oxides followed by a thermal treatment at low temperatures. The synthesized electrocatalysts are based on a combination of La, Mn, and Co oxides and hydroxides mixed with carbon black for oxygen electrochemical reactions. This work compares the electrocatalytic activity of the materials obtained at low temperatures using the hydrothermal approach with those prepared after a thermal treatment at high temperature. In addition, we also analyze the effect of a metal oxide structure stabilizer such as lanthanum in the synthesized metal (hydro-)oxides electrocatalysts and the effect of the carbon material in the electrocatalytic activity. Finally, the performance of the best electrocatalysts is studied in a rechargeable Zn-air battery.

2. Experimental

2.1. Materials and reagents

The reagents used in this work included Vulcan XC-72R carbon black (Vulcan) from Cabot Corporation, potassium hydroxide (KOH) from VWR Chemicals (85 % purity), ethanol (C_2H_5OH) from Alfa Aesar (99.5 % purity), isopropanol from Acros Organics (99.5 % purity), Nafion® 5% w/w, lanthanum(III) nitrate hexahydrate ($La(NO_3)_3{\cdot}6H_2O$) from Sigma Aldrich (99.9 % purity), manganese(II) nitrate tetrahydrate ($Mn(NO_3)_2{\cdot}4H_2O$) from Alfa Aesar (98 % purity), cobalt(II) nitrate hexahydrate ($Co(NO_3)_2{\cdot}6H_2O$) from Sigma Aldrich (99.9 % purity), and hexadecyltrimethylammonium bromide (CTAB) ($CH_3(CH_2)_{15}N(Br)(CH_3)_3$) from Sigma Aldrich (99.9 % purity). Additionally, Zn foil from ThermoScientific was used with a purity of 99.98 %, and zinc acetate dihydrate ($Zn(O_2CCH_3)_2{\cdot}2H_2O$) from Sigma Aldrich with a purity of 98 %. Commercial Pt/C (Sigma-Aldrich, 98 % purity) and RuO_2 (ThermoScientific, 99.95 % purity, sub-micron powder, surface area 45–65 m^2/g) were also utilized for comparison purposes. All solutions were prepared using ultrapure water (18 MΩ cm, Millipore® Milli-Q® water). The gases used, N_2 (99.999 %), O_2 (99.995 %), and H_2 (99.999 %), were provided by Carburos Metálicos and were used without any pretreatment.

2.2. Synthesis procedure

First, 6 mmol of each metal precursor are mixed in 30 ml of ultrapure water (Co is always introduced in 30 % of the Mn amount), and the surfactant CTAB is added in a 1:50 ratio with respect to the total metal content. Several combinations are tested such as La/Mn/Co, La/Mn, Mn/Co and Mn. Metal hydroxides are formed by adding drops of 6 M KOH to the solution until a pH ≈ 14 is reached, and then the solution is stirred for 18 h to ensure proper hydroxide formation. The solution is transferred to the autoclave, which is heated in an oven at 180 °C for 48 h. Subsequently, the autoclave is cooled in an ice bath. Then, the material is washed, filtered, and dried at 100 °C. Finally, depending on the type of sample, it is calcined at 200 or 600 °C for 6 h. The as-obtained samples are mixed with Vulcan by ball milling (Retsch PM 200 planetary ball-mill) for 30 min and 350 rpm, because these are the optimal conditions for ORR/OER electrocatalyst preparation, as previously reported [24]. The samples are named X-Y, where X is the metal used in the precursor and Y is the calcination temperature used after hydrothermal treatment; and if they are mixed with Vulcan, C letter is added: X-Y-C. The lanthanum precursor sample studied will be the one calcined at 200 ºC after hydrothermal treatment and will be denoted "La".

2.3. Characterization techniques

X-ray diffraction (XRD) analysis was performed using a Bruker D8-Advance diffractometer (Billerica, USA) equipped with a Goebel mirror for non-planar samples and an X-ray generator KRISTALLOFLEX K 760–80F (power: 3000 W, voltage: 20–60 kV, current: 5–80 mA) with a Cu Kα radiation source. XRD measurements were conducted over the 2θ range from 10 ° to 80 °, with a step size of 0.05 °. To estimate the size of the crystallites (Dc) in the materials, the Scherrer equation (Eq. (1)) was used [25].

$$D_c = \frac{k\lambda}{\beta\cos(\theta)} \tag{1}$$

In this equation, the constant (k), related to the grain shape, had a value of 0.89, and the wavelength of the radiation source (λ) used was 0.15406 nm. The full width at half maximum (FWHM) of the diffraction peak (β) and the Bragg angle (θ) were also involved in the calculation. By using a crystalline quartz pattern as a reference, the instrumental broadening factor was subtracted from the measured FWHM value. The corrected FWHM value of the sample was determined according to the following equation [25]:

$$\beta_{real}^2 = \beta_{obs}^2 - \beta_{inst}^2 \tag{2}$$

where β_{real} is the value obtained from the contribution of the crystallite size, β_{obs} is the measured value, and β_{inst} is the broadening related to the instrument.

The X-ray photoelectron spectroscopy (XPS) experiments were performed using a VG-Microtech Multilab 3000 electron spectrometer (VG Scientific, Sussex, UK). The spectrometer was equipped with a hemispherical electron analyzer featuring nine channeltrons with a passing energy range of 2–200 eV. The XPS measurements utilized an X-ray source emitting Al radiation (Kα 1253.6 eV). The C 1 s peak at 284.6 eV was used as an internal standard for bond energy determination. The XPS data were analyzed and deconvoluted using the XPSPEAK41 program. Experimental curves were fitted using Lorentz-Gaussian functions, and the background was modeled as a Shirley line.

Scanning electron microscopy (SEM) was used for the analysis of the sample morphologies using a JEOL model IT500HR/LA. This microscope is equipped with a field emission gun, providing high resolution (1.5 nm at 30 kV, and 4.0 nm at 1 kV), and it can operate within a voltage range from 0.5 to 30 kV.

The different synthesized materials were subjected to temperature programmed reduction (TPR) analysis using a Micromeritics Pulse Chemisorb 2705 instrument with a thermal conductivity detector (Norcross, GA, USA). The TPR process involved exposing the materials to a mixture of 5 vol% H_2 in Ar (35 mL/min) and increasing the temperature at a rate of 10 °C/min until reaching 950 °C.

The electrolyte employed in the electrochemical experiments was analyzed using Inductively Coupled Plasma Mass Spectrometry (ICP-MS) with a triple quadrupole Agilent model 8900. A He flow of 5 mL/

min was utilized, and three replicates of the sample were performed.

The electrocatalytic activity measurements were conducted using an Autolab PGSTAT302 potentiostat (Metrohm, The Netherlands). The electrochemical characterization involved cyclic voltammetry measurements in an N_2-saturated atmosphere using a 0.1 M KOH solution at a scan rate of 50 mV/s. A rotating ring-disk electrode (RRDE) from Pine Research Instruments, USA, was utilized as the working electrode. This RRDE consisted of a glassy carbon disk electrode with a diameter of 5.00 mm, along with an attached platinum ring. Inks of the different electrocatalysts were prepared by sonicating a suspension containing 1 mg of the electrocatalysts and 1 mL of a solution consisting of 0.02 vol% Nafion® and 20 vol% isopropanol in water. Then, 100 µL of this dispersion was deposited on the glassy carbon electrode. The counter electrode used was made of graphite, while the reference electrode was a reversible hydrogen electrode (RHE) immersed in the working electrolyte through a Luggin capillary.

Electrocatalytic activity towards the ORR (oxygen reduction reaction) was investigated by linear sweep voltammetry (LSV) in an O_2-saturated 0.1 M KOH solution, scanning from 1.0 to 0.0 V (vs. RHE) at different rotation rates, ranging from 400 to 2025 rpm, and at a scan rate of 5 mV/s. During all experiments, the potential of the Pt ring electrode was maintained constant at 1.5 V (vs. RHE). The quantification of the electron transfer number was determined from the currents of the disk and the ring electrodes using the following equation (Eq. (3)):

$$n_{e^-} = \frac{4|\mathrm{I_d}|}{|\mathrm{I_d}|+|\mathrm{I_r}|/\mathrm{N}} \tag{3}$$

where I_r represents the current measured on the ring electrode, I_d represents the current measured on the disk electrode, and N is the efficiency of ring collection, which was found to be 0.26. Moving on to the OER experiments, they were carried out using the RRDE setup and linear sweep voltammetry (LSV) scans from 1 to 1.8 V (vs. RHE) in an N_2-saturated atmosphere. The rotation rate during these experiments was set at 1600 rpm, and the scan rate was maintained at 5 mV/s. The experiments were conducted using a 0.1 M KOH solution. The ORR and OER kinetics were evaluated using Tafel plots, $\eta = a + b\ log(j)$ where η is the overpotential and j is the current density [26]. These analyses have been conducted within a region controlled by the electron transfer reactions and the potential range employed in each case was chosen near to E_{ONSET}, not exceeding 20 mV, until achieving a linear relationship. Moreover, stability tests were conducted with freshly prepared electrodes, for both ORR and OER, and glassy carbon was used as the substrate for further XPS analysis. For the ORR stability chronoamperometric test, a constant potential of 0.65 V vs RHE was maintained for 3 h. On the other hand, the OER stability test involved performing up to 2000 cycles between 1.0–1.8 V vs RHE.

2.4. Rechargeable Zn-air battery

The testing of the rechargeable zinc-air battery (ZAB) used the setup depicted in Fig. S1. The positive air electrodes consisted of the most promising electrocatalysts developed in this study and a commercial 20 wt.% Pt/C + RuO_2 (1:1 weight ratio) catalyst ink (0.02 vol% Nafion® and 20 vol% isopropanol in water). These materials were evenly applied to a gas diffusion layer carbon paper (QUINTECH, Freudenberg H23C6) until achieving a mass loading of 1.3 mg/cm^2. The negative electrode was a polished Zn foil (ThermoScientific, 99.98 %). The electrolyte used was an aqueous solution comprising 6 M KOH + 0.2 M $Zn(O_2CCH_3)_2$. The electrodes had a geometrical area of 2.6 cm^2. Battery tests were conducted using an ARBIN multi-channel SCTS battery testing potentiostat. Polarization curves were obtained at a scan rate of 1 mA/s. Galvanostatic discharge and charge measurements were obtained with 1 mA/cm^2 and 20-min charge-discharge cycle.

3. Results and discussion

3.1. Crystal structure characterization by XRD

Fig. 1 shows the XRD patterns of the different metal oxides synthesized. According to crystallographic databases, the sample obtained with the lanthanum precursor (La sample) results in crystalline lanthanum hydroxide ($La(OH)_3$) (#96–403–1382). In the case of Mn-200 sample, crystalline phases associated mainly with hausmannite (Mn_3O_4) (#96–101–1263) and a small contribution from crystalline MnO_2 phase (#96–151–4026) are obtained. The Mn-600 sample shows different crystalline peaks than Mn-200, which can be related mainly to the bixbyite phase (Mn_2O_3) (#96–101–0899) as well as hausmannite. Furthermore, Mn/Co-200 and Mn/Co-600 samples show diffractograms typical of low crystallinity/amorphous samples due to the absence of sharp and intense peaks. However, their crystalline diffraction peaks are associated with the manganese-cobalt double oxide $CoMn_2O_4$ (#96–210–6724). In the case of La/Mn/Co-200 sample, a diffractogram similar to the La sample is obtained, associated with high crystallinity of $La(OH)_3$ phase, as well as some low-crystallinity peaks associated with hausmannite. The fact that additional Mn or Co-related peaks are not observed may be due to the high crystallinity of $La(OH)_3$, which overlaps the contribution from low-crystallinity species. Finally, the XRD for La/Mn/Co-600 sample is associated with the perovskite-type phase $LaMnO_3$ (#96–154–2146). It should be emphasized that the structure of $LaMnO_3$ is preserved in the perovskite because the amount of Co in its structure is not sufficient to change it, although the theoretical expected perovskite is $LaMn_{0.7}Co_{0.3}O_3$ due to the ratio between manganese and cobalt precursors; this observation is consistent with previous studies [27]. It must be noted that the ball milling treatment with the carbon material (La/Mn/Co-200-C and La/Mn/Co-600-C samples) does not change the crystalline phases of the metal oxides (Fig. S2), but the crystal size decreases (Table 1). Therefore, the obtained samples show variable crystallinity and composition, which may greatly affect the electrocatalytic activity.

Moreover, the La/Mn-200 and La/Mn-600 samples were also synthesized to compare their behaviour with that of La/Mn/Co-200 and La/Mn/Co-600 samples (Fig. S3). The La/Mn-200 sample contains high crystallinity lanthanum hydroxide, as observed for La/Mn/Co-200 sample. Furthermore, XRD for La/Mn-600 and La/Mn/Co-600 samples are associated with $LaMnO_3$ perovskite structure, as expected. Table 1 shows the crystal size (Dc) determined for all samples. It can be observed that the values are close to ~30 nm for all samples except for La and perovskite-type materials, where crystal sizes of 14 and 21 nm are obtained, respectively. It is interesting to note that La/Mn/Co-200 sample

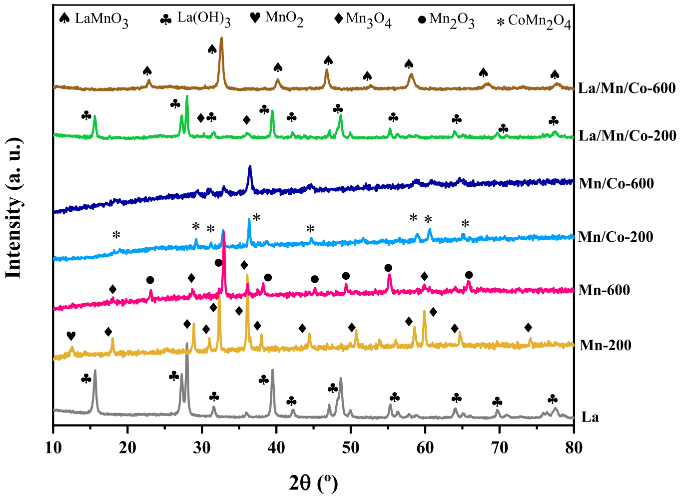

Fig. 1. X-Ray diffraction patterns of the synthesized metal oxides.

Table 1
Average crystallite size for the synthesized metal oxides obtained from XRD patterns in Fig. 1.

Sample	Dc (nm)
La	14
Mn-200	30
Mn-600	29
Mn/Co-200	30
Mn/Co-600	30
La/Mn/Co-200	29
La/Mn/Co-200-C	26
La/Mn/Co-600	21
La/Mn/Co-600-C	19
La/Mn-200	30
La/Mn-600	20

shows a similar crystal size to the other metal oxides, although its main crystalline phase is associated with that of La sample, which has a crystal size of 14 nm. Furthermore, a decrease in crystallite size is observed in samples with a perovskite-type structure (La/Mn/Co-600 and La/Mn-600) compared to calcination at 200 °C. This phenomenon is associated with the significant phase transformation occurring during the calcination process.

3.2. Characterization by XPS

Fig. 2 displays Mn 2p, La 3d, Co 2p and O 1 s XPS spectra of the different metal oxides samples in presence of carbon material. Fig. 2A shows the spectra of Mn 2p for all samples mixed with Vulcan. They present two spin-orbit coupling signals at around 642.5 and 655.0 eV corresponding to $2p_{3/2}$ and $2p_{1/2}$, respectively. In all samples, the Mn $2p_{3/2}$ peak can be deconvoluted into three peaks at 640.8, 642.2 and 644.0 eV, which correspond to Mn(II), Mn(III) and Mn(IV) species, respectively [28]. Similarly, the $2p_{1/2}$ peak can be deconvoluted into three peaks at 652.3, 653.7 and 655.5 eV, which are associated with Mn (II), Mn(III) and Mn(IV) species, respectively. The results show the presence of the three oxidation states at the surface of the materials, of which Mn(III) is the predominant one, and the amount of the other oxidation states depend on the sample. Mn-200-C presents a higher Mn (II) content than Mn-600-C, in agreement with the XRD results since Mn-200-C is associated with the Mn_3O_4 structure, whereas Mn-600-C is predominantly associated with Mn_2O_3. Furthermore, sample Mn/Co-200-C shows a low Mn(II) content compared with Mn-600-C and Mn/Co-600-C, due to the larger content of Mn species with higher degree of oxidation, such as Mn(IV) species; when the Mn/Co-200-C sample undergoes a heat treatment at an elevated temperature (Mn/Co-600-C sample), the amount of Mn(II) species increases with respect to Mn(IV) species. Therefore, it can be stated that the addition of Co in the hydrothermal synthesis and calcination at low temperatures does not favor the formation of Mn(II) species in the crystalline mixed oxide Mn_2CoO_4. In addition, La/Mn/Co-200-C sample has a lower Mn (II) content than La/Mn/Co-600-C, although it is higher than that of Mn/Co-200-C sample. Then, thermal treatment increases the amount of Mn(II) species and decreases the content of Mn(IV) species (La/Mn/Co-600-C sample). In summary, it can be confirmed that there are differences in the oxidation states of manganese, depending on the thermal treatment and the precursors used, which can affect the electrocatalytic activity.

XPS of lanthanum shows a complex shape with high intensity satellite peaks which complicate deconvolution [29]. The intensity and energy separation of the satellites relative to the main peak are highly

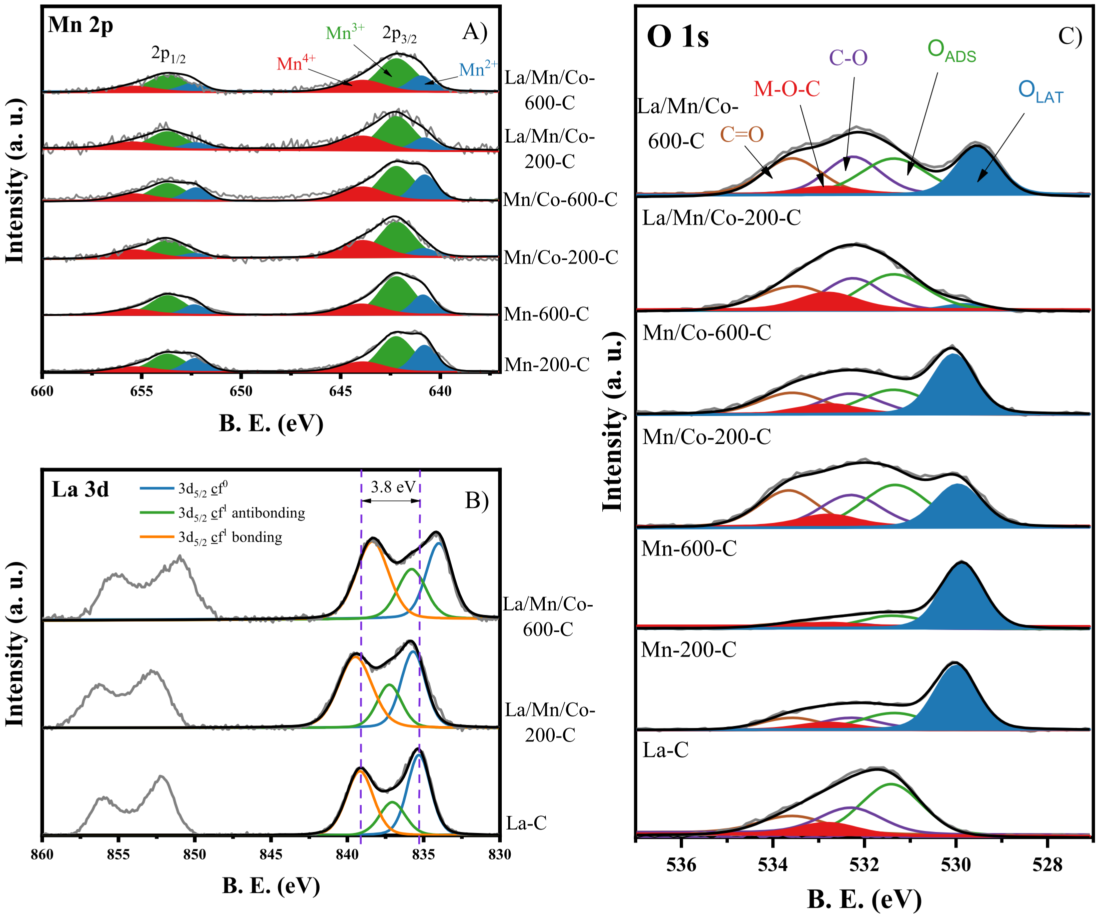

Fig. 2. XPS spectra of A) Mn 2p, B) La 3d and C) O 1 s, for the different electrocatalysts.

sensitive to the ligand atoms. Charge transfer from the ligand atom to the ionized $4f^0$ orbital of the core lanthanum atom was suggested to be the origin of the observed complex photoelectron peak structures [30]. Fig. 2B shows the La 3d spectra, where two regions can be seen at ~836 and ~853 eV corresponding to La $3d_{5/2}$ and $3d_{3/2}$, respectively. In the case of La $3d_{5/2}$ region, two peaks are observed which separation is ~3.8 eV for the La-C and La/Mn/Co-200-C samples, which is related to the presence of $La(OH)_3$ species [31], in agreement with the XRD results. This region can be deconvoluted into three contributions. The peak at ~835.2 eV is associated with electron transfer to the empty $4f^0$ orbital, and the other two are associated with the transition of an electron from the ligand to the anti-bonding (~837.1 eV) and bonding (~839.2 eV) orbitals of lanthanum. In the La/Mn/Co-600-C sample, the peak separation at La $3d_{5/2}$ is ~4.2 eV corresponds to La(III) in the perovskite-type structure [27]. Using the La-C sample as a reference, the La/Mn/Co-200-C sample peak is shifted to higher binding energies and the La/Mn/Co-600-C sample peak to lower ones; these observations reveal the differences in the environment for the lanthanum species in the different samples. This could be related to different electronic interactions between Mn and Co with La.

The O 1 s spectra for all samples mixed with Vulcan is shown in Fig. 2C. The O 1 s spectrum can be deconvoluted into five peaks considering the contributions from the carbon material and those from the metal (hydro-)oxide. Several peaks are observed at ~530.0, ~531.4, ~532.3, ~532.8 and ~533.6 eV, corresponding to lattice oxygen (O^{2-}), O—H species and adsorbed oxygen species such as O_2^- and O_2^{2-}, C—O of the carbon material, M-O-C species caused by the interaction between the carbon material and the metal species, and C = O species of the carbon material, respectively [28,32–34]. The absence of a peak at 530.0 eV corresponding to lattice oxygen in the La-C and La/Mn/Co-200-C samples is the most significant difference between all samples (Fig. 2C), which is consistent with the XRD results showing that these samples are mainly associated with the $La(OH)_3$ crystalline phase. The manganese and cobalt phases in La/Mn/Co-200-C are associated with metal hydroxides. The binding energy at which lattice oxygen appears is shifted depending on the metallic environment; for instance, the lattice oxygen in Mn/Co-C samples appears at binding energies similar to those in only manganese-containing samples. In all materials, the M-O-C interaction produced by ball milling between the metal-containing compounds and the carbon material, is observed. The presence of the M-O-C interaction has been associated with enhanced electrochemical activity [24,35,36], and this contribution is higher in the La/Mn/Co-200-C sample.

Finally, Fig. S4 presents the Co 2p spectra of the Mn/Co-200-C and Mn/Co-600 samples. The Co $2p_{3/2}$ peak can be deconvoluted into two peaks at 780.4 and 782.4 eV, corresponding to Co(III) and Co(II) species, respectively [37], and the Co $2p_{1/2}$ peak can be deconvoluted into peaks at 795.5 and 797.4 eV, corresponding to Co(III) and Co(II), respectively. In both samples, a mixture of Co(III) and Co(II) oxidation states with a similar contribution is obtained. Thus, there is no modification of the

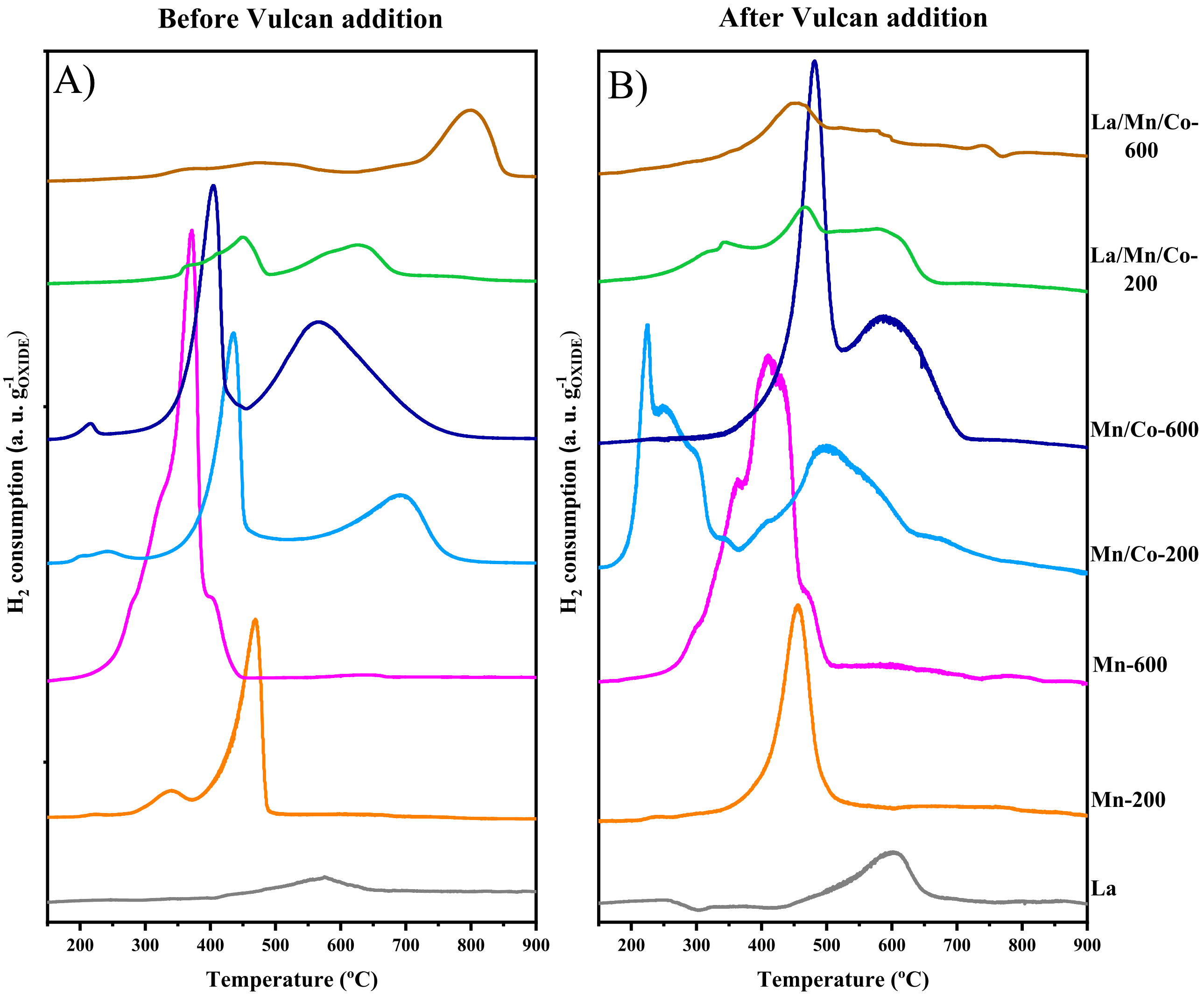

Fig. 3. TPR-H_2 profiles for the electrocatalysts A) before and B) after Vulcan addition normalized per gram of oxide in order to compare the two figures.

oxidation state of the cobalt species with the high-temperature heat treatment, unlike in the case of manganese. Fig. S5 shows the Co 2p spectra for La/Mn/Co-200-C and La/Mn/Co-600 samples, where two main peaks are observed at ~781.6 and ~796.8 eV, corresponding to Co $2p_{3/2}$ and Co $2p_{1/2}$, respectively [38]. However, the low amount of Co in these last samples makes the deconvolution of the XPS peaks difficult.

3.3. Characterization by TPR

Fig. 3 shows the TPR-H_2 profiles of the metal (hydro-)oxides (Fig. 3A), and these materials after mixing with carbon black using the ball-milling method (Fig. 3B). It is important to distinguish between these two kinds of samples because the addition of the carbon material strongly affect the TPR profile of the metal oxide, due to the interaction with the carbon material. Significant differences are observed in the metal oxides, both with and without the addition of the carbon material. Regarding metal oxide electrocatalysts without carbon material (Fig. 3A), the sample La shows a small reduction peak at ~570 °C, which is associated with the reduction of La(III) to La(II) [39]. Mn-200 and Mn-600 samples show a prominent hydrogen consumption peak at ~450 °C and ~350 °C, respectively, which is associated with the reduction of manganese species to form MnO [40,41]. The peak of the Mn-600 sample is more intense and appears at a lower temperature due to the higher amorphous nature of the sample [42]. Moreover, this peak is larger due to a higher content of Mn(IV) species.

The hydrogen consumption profiles for Mn/Co-200 and Mn/Co-600 samples exhibit two main peaks, the first one, which appears at a temperature lower than 450 °C, can be associated with the reduction of the MnO_2 and Mn_2O_3 species to Mn_3O_4 and Co_3O_4 to CoO; and the second one, at temperatures higher than 500 °C, with the reduction of Mn_3O_4 and CoO to MnO and metallic Co, respectively [41,43]. The main difference between these two samples is that the reduction peaks appear at a lower temperature in Mn/Co-600 sample, which could be related to the differences in the manganese oxidation states, as reported by XPS analysis. Moreover, significant differences are observed for La/Mn/Co-200 and La/Mn/Co-600 samples. La/Mn/Co-200 sample shows two main peaks at ~450 and ~620 °C which can be associated with the reduction of the same species as the Mn/Co samples due to their similarity in both shape and temperature range. The perovskite-type sample La/Mn/Co-600 presents a major peak at ~800 °C which is related to the reduction of Mn(III) to Mn(II) overlapped with the reduction of Co(II) to Co(0) [44]. Thus, the significant differences between the La/Mn/Co-200 and La/Mn/Co-600 samples in terms of structure and reducibility of the component species can be clearly detected from TPR-H_2.

When the materials are mixed with the carbon material important changes occur depending on the material. Thus, the peaks are shifted to lower temperatures for the Mn/Co-200 sample and to higher temperatures for the Mn/Co-600 sample, this is related with changes in the reducibility of the cations. The hydrogen consumption profile of the La/Mn/Co-600 and La/Mn/Co-200 samples mixed with carbon material shows significant changes in shape and in H_2 consumption after addition of Vulcan. It is detected the appearance of a single peak at 450 °C in La/Mn/Co-600-C sample associated with the reduction of Mn(III) to Mn(II), as previously reported for Perovskite-Carbon composites [24,35]. The reduction peak of Mn-600 sample is also affected by the addition of the carbon material appearing at higher temperature, although this effect is less pronounced than in the case of Mn/Co-600 sample. La and Mn-200 samples do not suffer significant modifications by the addition of carbon material. Therefore, it has been observed that metal oxides prepared at high temperatures exhibit important changes in the TPR-H_2 profile compared to those obtained at low temperatures. This is a consequence of a different interaction with the carbon material. Thus, important differences in the electrocatalytic activity are expected among these materials.

3.4. Morphological characterization

Fig. 4 presents the SEM images of the as-synthesized catalysts by the hydrothermal method and subsequent calcination at 200 and 600 °C. The Mn-200 samples are generally formed by irregular cuboids of length ~1 μm and other polyhedral shapes of similar size, generating sponge-shaped nanostructures. The Mn-600 sample shows similar morphological characteristics, although thermal treatment produces nanorods and clusters of length ~1 μm. Furthermore, the Mn/Co-200 sample differs from the previous ones, and it consists of regular agglomerated nanoparticles of cubic structure with a size of less than ~1 μm; while in the high temperature Mn/Co-600 sample, the heat treatment causes the particles to sinter, thus increasing their size to ~2 μm and losing their regular structure. The large difference observed between the Mn and Mn/Co samples is due to the introduction of Co, as it has a large effect on the morphology of manganese and cobalt mixed oxides [45].

The La/Mn/Co-200 sample is composed of fractured nanorods of length less than 1 μm, similar to the La sample (Fig. S6). No distinct structures associated with the manganese and cobalt species were observed; thus, lanthanum seems to favour the formation of nanorods. Regarding the La/Mn/Co-600 sample, it contains perovskite particles of variable polyhedral shape. The particles have a size of less than 1 μm. In this case, some nanorods with a length of ~4 μm are also observed, presumably facilitated by the presence of lanthanum.

3.5. Electrochemical characterization toward ORR/OER

Fig. 5 shows the cyclic voltametric profiles obtained in nitrogen atmosphere in alkaline electrolyte. Fig. 5A includes the results for the catalysts calcined at 200 °C and Fig. 5B for the materials prepared at 600 °C. The La-C sample shows a voltammogram of capacitive character with the absence of redox processes in the potential window studied, in agreement with the literature [46]. Moreover, the voltametric charge is the smallest for the samples studied. For Mn-200-C sample, the voltammogram shows the presence of redox peaks with the anodic wave at 1.1 V and the cathodic one at around 0.8 V, corresponding to the Mn (II)/Mn(III) redox process [14,47]. This is also observed for the Mn-600-C sample but with, both, higher intensity of the anodic peak and higher irreversibility of the redox process; these differences among samples are associated with the phase change resulting from the applied thermal treatment. This behavior changes in La/Mn/Co-200-C sample, where two overlapped redox peaks are observed in the anodic regions at 0.5 V and 1.0 V respectively, which agrees with the literature for perovskite-type metal oxides [48]. These peaks are related with Mn (II)/Mn(III) redox process although the peak at ~1.0 V can also correspond to the Co(II)/Co(III) redox pair [49], which appears overlapped with the latter. La/Mn/Co-600-C sample shows these two overlapping redox processes, but the voltametric charge decreases. Regarding the Mn/Co-200-C and Mn/Co-600-C samples, the first one shows a wide anodic peak at higher potentials (around 1.2 V), which can correspond to the overlapping of the manganese and cobalt redox processes, while Mn/Co-600-C shows this peak at 1.0 V. The shift of this peak towards higher potentials may be due to differences in the oxidation states of the cations, as detected by XPS (lower Mn(II) content) which modifies the electronic environment.

The different metal (hydro-)oxides-carbon composites have been studied in ORR. Fig. 6 shows the LSV curves obtained in an O_2 saturated solution, and Table 2 summarizes the electrochemical parameters obtained from these curves. La-C sample has a low electroactivity for this reaction, with an onset potential (E_{ONSET}) of 0.72 V determined at −0.10 mA/cm^2 [50] and, a limiting current density of −2.3 mA/cm^2 at 0.2 V. Fig. 6A compares the different materials calcined at 200 °C and La/Mn/Co-600-C sample. It can be observed that the La/Mn/Co-200-C and Mn-200-C samples present a high E_{ONSET} of 0.86 V, but only La/Mn/Co-200-C reaches a high limiting current density at 0.2 V (−4.6 mA/cm^2 in comparison to −3.8 mA/cm^2 for Mn-200-C). Mn/Co-200-C

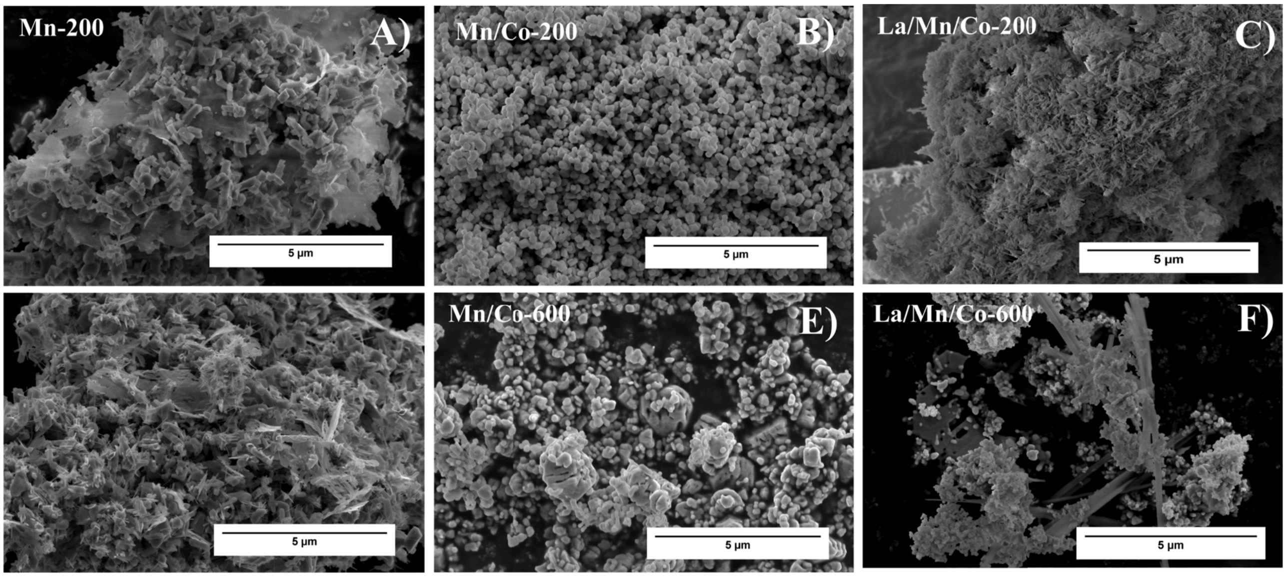

Fig. 4. SEM images of the metal (hydro-)oxides: A) Mn-200, B) Mn/Co-200, C) La/Mn/Co-200, D) Mn-600, E) Mn/Co-600 and F) La/Mn/Co-600.

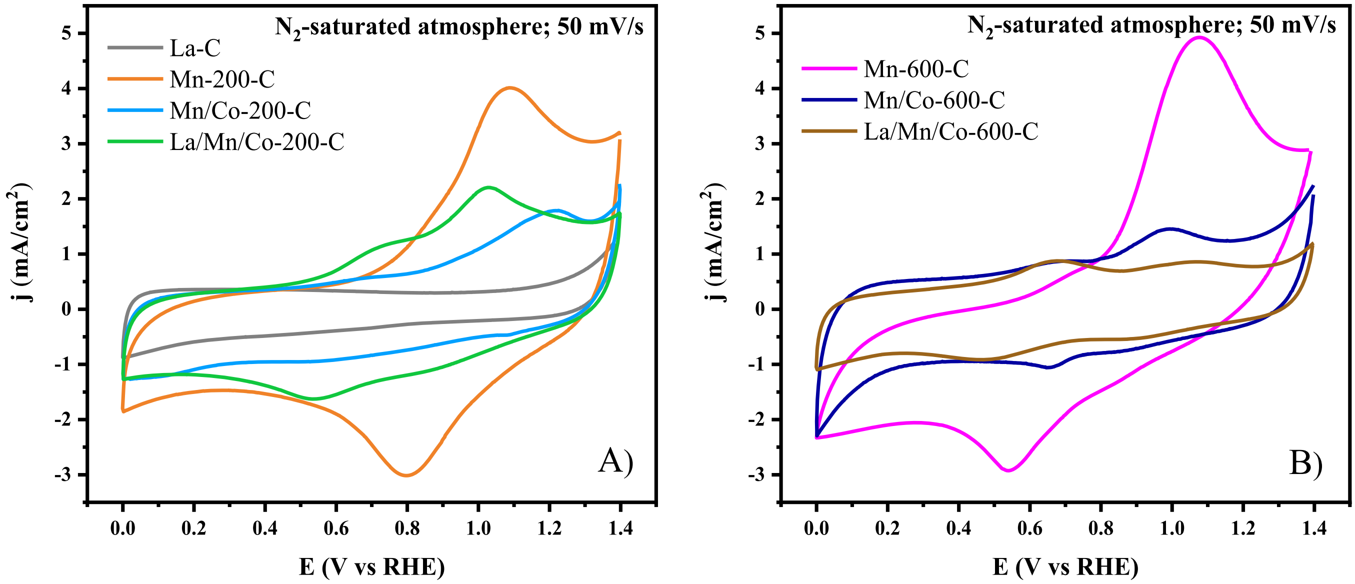

Fig. 5. Cyclic voltammograms in 0.1 M KOH solution in saturated N_2 atmosphere, $v = 50$ mV/s, for calcined temperatures of A) 200 °C and B) 600 °C.

sample also shows a high E_{ONSET}, with a value of 0.85 V and a limiting current density similar to that of La/Mn/Co-200-C. Finally, the La/Mn/Co-600-C perovskite-type sample, shows the lowest E_{ONSET} compared to those calcined at 200 °C, and the limiting current density is also lower at 0.2 V. Fig. 6B compares the samples calcined at 600 °C with the La/Mn/Co-200-C sample, which shows a high E_{ONSET} compared to the other materials, and all these samples show similar limiting current densities. It can therefore be concluded that heat treatment at 200 °C after hydrothermal treatment is more appropriate than heat treatment at 600 °C for achieving higher electrocatalytic activity for this reaction.

Mn-600-C sample shows a lower E_{ONSET} than its corresponding material prepared 200 °C; this can be in agreement with the observed shift of the Mn(III)/Mn(II) reduction peak towards lower potentials (Fig. 5), as it has been shown that the catalytic activity is enhanced if the active metal has redox processes in the region close to the E_{ONSET} [51,52]. Moreover, the limiting current density of the Mn-600-C sample has been considerably improved, reaching a value of -4.6 mA/cm^2. The Mn/Co-600-C sample shows a similar electrochemical activity to ORR than Mn/Co-200-C sample.

Fig. 6C plots the number of electrons transferred determined in the ORR. It can be observed that in all the electrocatalysts the values are close to 4 except for Mn-200-C sample which is close to 3 (Table 2). The La/Mn/Co-200 sample is the one that presents a reaction path closer to 4 electrons (3.6 at 0.4 V), which improves the value of La/Mn/Co-600-C electrocatalyst (3.3 transferred electrons). Moreover, one potential issue when using the rotating disk-ring electrode in an alkaline medium, where the Pt ring potential is maintained at 1.5 V vs RHE, is the possible dissolution [53] of Pt and redeposition on the working electrode, thereby enhancing its performance. To verify that this does not affect electrocatalytic results, the electrolyte was analyzed via ICP-MS after a 3-hour stability experiment (to be explained later), revealing no significant presence of Pt (Table S1). Additionally, an ORR experiment was conducted with the La/Mn/Co-200-C sample on a rotating disk-ring electrode without the ring (Fig. S7), yielding highly similar results. This confirms that the electrocatalytic activity of the materials is not being influenced by this aspect.

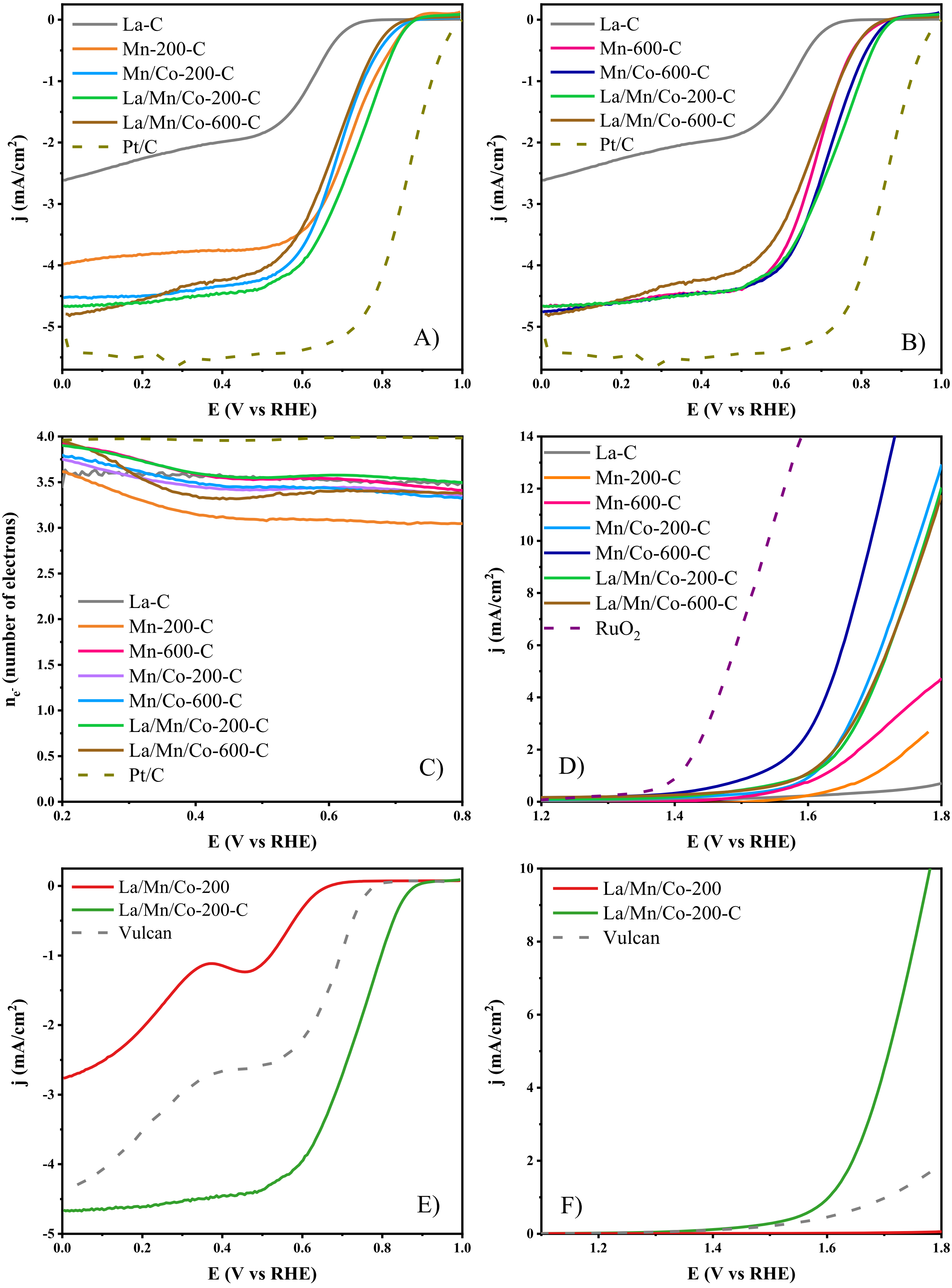

Fig. 6. LSV for ORR in 0.1 M KOH saturated with O_2 at 1600 rpm for samples calcined at A) 200 °C and B) 600 °C. C) Number of electrons transferred to the ORR. D) LSV for OER in 0.1 M KOH saturated with N_2 at 1600 rpm. LSV for La/Mn/Co-200, La/Mn/Co-200-C and carbon material samples for E) ORR and F) OER. Scan rate for all the experiments: 5 mV/s.

Table 2
ORR and OER electrochemical parameters obtained in the LSV curves for the metal (hydro-)oxides-carbon electrocatalysts.

Sample	**ORR**				**OER**			
	E_{ONSET} / V (at -0.10 mA/cm^2)	n_e^- (at 0.4 V)	*j*/ mA/cm (at 0.2 V)	**Tafel slope** (mV/dec)	**Potential / V (at 1 mA/cm^2)**	**Potential / V (at 10 mA/cm^2)**	**Tafel slope (mV/dec)**	**BI/ V**
La-C	*0.72*	*3.6*	*−2.3*	*66*	–	–	–	–
Mn-200-C	*0.86*	*3.1*	*−3.8*	*100*	*1.70*	–	*177*	*0.84*
Mn-600-C	*0.83*	*3.6*	*−4.6*	*81*	*1.61*	–	*255*	*0.78*
Mn/Co-200-C	*0.85*	*3.4*	*−4.5*	*79*	*1.62*	*1.75*	*125*	*0.77*
Mn/Co-600-C	***0.85***	***3.5***	***−4.6***	***71***	***1.52***	***1.69***	***172***	***0.67***
La/Mn/Co-200-C	***0.86***	***3.6***	***−4.6***	***73***	***1.60***	***1.78***	***156***	***0.74***
La/Mn/Co-600-C	*0.83*	*3.3*	*−4.6*	*70*	*1.59*	*1.73*	*153*	*0.76*
La/Mn-200-C	*0.79*	*2.9*	*−3.8*	*76*	*1.65*	–	*204*	*0.86*
La/Mn-600-C	*0.82*	*3.3*	*−4.3*	*82*	*1.64*	–	*221*	*0.85*
La/Mn/Co-200	*0.73*	*3.4*	*−2.1*	*69*	–	–	–	–
Pt/C	*0.98*	*4.0*	*−5.5*	*61*	–	–	–	–
RuO_2	–	–	–	–	*1.40*	*1.54*	*103*	–

Fig. 6D contains the LSVs performed to evaluate the OER for the different electrocatalysts in a N_2-saturated atmosphere at 1600 rpm. The results show the outstanding electrochemical activity of the Mn/Co-600-C sample for this reaction, with an E_{ONSET} (determined at 1 mA/cm^2 [54]) of 1.52 V and a potential at 10 mA/cm^2 of 1.75 V. Mn/Co-200-C sample also exhibits good electrochemical activity to OER in comparison to the other samples. These results can be explained considering that these two electrocatalysts possess a higher content of Co, which is more active for OER [55]. Manganese-containing samples, Mn-200-C and Mn-600-C, present a low electrochemical activity for this reaction, and do not reach 10 mA/cm^2 in the potential window studied. Finally, the La/Mn/Co-200-C and La/Mn/Co-600-C samples show E_{ONSET} potentials of 1.60 and 1.59 V respectively, and potentials of 1.78 and 1.73 V at 10 mA/cm^2, respectively. These higher values compared to the Mn/Co-200-C and Mn/Co-600-C materials may be due to the smaller presence of cobalt in these materials.

Due to the outstanding bifunctional activity of the La/Mn/Co-200-C sample, electrochemical performance of the La/Mn-200-C and La/Mn-600-C materials was analyzed for comparison purposes (Fig. S8). In these samples, both the ORR and the number of electrons transferred are lower. This may be because lanthanum adequately stabilises the manganese-cobalt mixed oxide ($CoMn_2O_4$) structure and generates the most adequate active sites for this reaction.

Figure S9 and Table 2 display the Tafel plots for both reactions. The Tafel analysis is a useful technique for studying processes that determine the rate of electron transfer [56]. Generally, smaller Tafel slopes indicate higher ORR/OER activities Then, the smaller Tafel slope value indicates that increasing the same current density would need smaller overpotential suggesting a faster reaction rate [26]. For the ORR, the obtained values are between 81 and 69 mV/dec, except for Mn-200-C catalyst, thus demonstrating the suitable kinetics occurring in these electrocatalysts in the ORR. Regarding OER, the smaller values of the Tafel slope are obtained for Mn/Co-200-C, La/Mn/Co-200-C and La/Mn/Co-600 samples. For the other samples, the values of Tafel slope are higher.

Fig. 6E and F show the LSV for ORR and OER, respectively, for the sample La/Mn/Co-200 with and without being mixed with Vulcan. Huge differences are observed in the electrocatalytic activity, demonstrating the importance of mixing metal oxides with carbon materials that provides better electrical conductivity, thus improving the electrochemical performance by a synergistic effect [35,57].

In order to study the bifunctionality of the materials, the so-called bifunctional index (BI) has been calculated (Table 2). This index is the difference between the E_{ONSET} potentials for ORR and OER reactions. Due to the extraordinary activity for OER of the Mn/Co-600-C sample, it is the one that has the best BI, followed by La/Mn/Co-200-C sample. It is remarkable the value obtained in the La/Mn/Co-200-C sample because a heat treatment at low temperature is used for the synthesis of the material. A possible explanation for the extraordinary bifunctional electrochemical activity of both samples may be related to the crystallinity of the material as obtained from X-ray diffraction. Mn/Co-600-C sample shows low crystallinity (Fig. 1) and La/Mn/Co-200-C has a diffractogram with peaks associated with crystalline $La(OH)_3$ and in which the manganese and cobalt-containing species have a low crystallinity or amorphous structure. It has been shown that the crystallinity of the metal oxides has a strong impact on the electrocatalytic activity; amorphous oxides present superior performance because of a higher number of active sites formed from lattice defects and/or improved ionic conductivity because of their abundant oxygen vacancies. Another critical factor is the oxidation state of the active metals for ORR/OER as determined by XPS; in general, there seems to exist a relationship between the presence of Mn (II) and an enhancement in the electrocatalytic activity for samples calcined at low temperature. Moreover, it is remarkable the extraordinary electrochemical activity of the La/Mn/Co-200-C sample even with the presence of lanthanum as $La(OH)_3$ (which does not show a good electrochemical activity); however, its presence modifies the surface morphology, making it similar to lanthanum hydroxide, and produced local structural changes such as the absence of lattice oxygen as observed by XPS, an aspect that is found in the rest of the samples except for the La sample. Another aspect that influences the electrocatalytic activity is the interaction of the metal (hydro-)oxides with the carbon material, represented by the M-O-C interaction in the XPS spectra. The sample with the highest contribution of this interaction is La/Mn/Co-200-C, which agrees with the results of the electrocatalytic activity.

3.6. Stability of the electrocatalysts

The long-term stability tests for ORR (Fig. 7A) and OER (Fig. 7B) of the La/Mn/Co-200-C sample, shows comparable results to the commercial Pt/C catalyst for ORR and adequate stability for OER up to 500 cycles. XPS was analyzed after the stability tests for these two experiments, showing significant differences in the La 3d spectra. After the OER test (Fig. 7C), the XPS peak shifts towards lower binding energies and there are differences in the contributions of the deconvoluted peak. In this sense, a decrease in the bonding contribution is detected after the OER test with respect to the initial one, which is compensated by an increase in the contribution of the empty f orbital. This may indicate a decrease in the interaction between lanthanum and manganese and cobalt ions, what is in agreement with the worsening of the electrocatalytic activity. After the ORR stability test, the XPS of the used sample does not present well defined peaks, indicating that there is a substantial change in the metallic environment, although it was found that the sample is still stable (Fig. 7A). Moreover, a similar ratio is observed

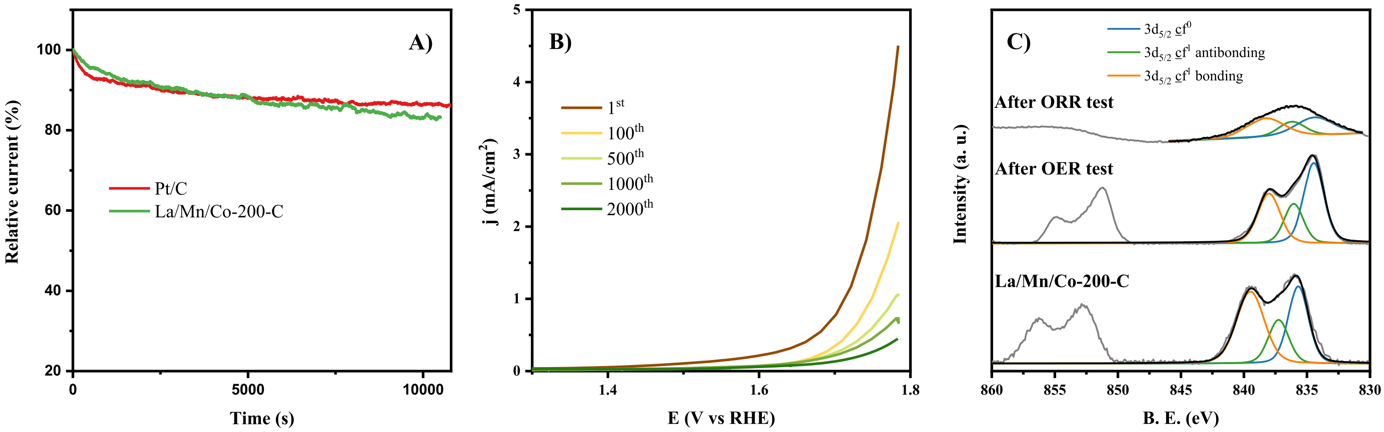

Fig. 7. A) Chronoamperometric ORR stability test for La/Mn/Co-200-C and commercial Pt/C samples. B) OER stability test for La/Mn/Co-200-C sample. C) XPS results after ORR chronoamperometric stability test for La/Mn/Co-200-C samples. D) XPS comparison after ORR chronoamperometric stability test for La/Mn/Co-200-C and La/Mn/Co-600-C.

between the contributions of the 3d$_{5/2}$ peak associated with the empty f orbital and the bonding one, which is similar to the original perovskite material.

To deepen into the interaction of La in the La/Mn/Co-200-C sample in the ORR, it will be compared with the perovskite-type sample (La/Mn/Co-600-C), because this is a stable material and has been extensively studied. Fig. S10 shows the La 3d spectra of these samples before and after the ORR stability test. As can be observed, the XPS does not change so significantly for the perovskite La/Mn/Co-600-C, except for a higher contribution of the empty f orbital in the used sample. In summary, lanthanum chemical environment suffers a noteworthy change only in the La/Mn/Co-200-C sample during ORR although this change does not deteriorate the stability (Fig. 7A). Regarding the O 1 s spectrum (Fig. S11), a decrease of the M-O-C and O$_{ADS}$ contributions is detected in the La/Mn/Co-200-C sample after the stability test compared to the initial sample; moreover, an increase of the C—O groups of the carbon material is observed. In the La/Mn/Co-600-C sample, the main difference is the decrease in the O$_{LAT}$ contribution in the used sample, although comparable results are obtained.

The cyclic voltammetry before and after performing the ORR has been studied for all samples (Fig. 8). Significant differences are detected for the Mn-200-C and Mn-600-C samples, where the voltametric charge decreases but the redox processes are maintained after the ORR, suggesting a decrease in the number of available active sites. For the Mn/Co-C and La/Mn/Co-C samples, the voltametric peaks remain relatively stable, but the profile changes in the case of Mn/Co-600 sample in which the two redox processes appear now as one at higher potentials. The change in the redox peak intensities in the La/Mn/Co-600-C sample after the ORR can be attributed to a change in the surface concentration of the electroactive species. The peaks at 0.7 and 1.0 V are associated with the Mn(II)/Mn(III) and Co(II)/Co(III) redox transitions, respectively. With the use of the sample, the charge associated to Mn(II)/Mn (III) decreases and that corresponding to Co(II)/Co(III) increases. Then, it seems that the amount of electroactive Co increases during the ORR. Moreover, La/Mn/Co-200-C sample essentially maintains the voltametric profile, thus the interaction between all the metal species seems

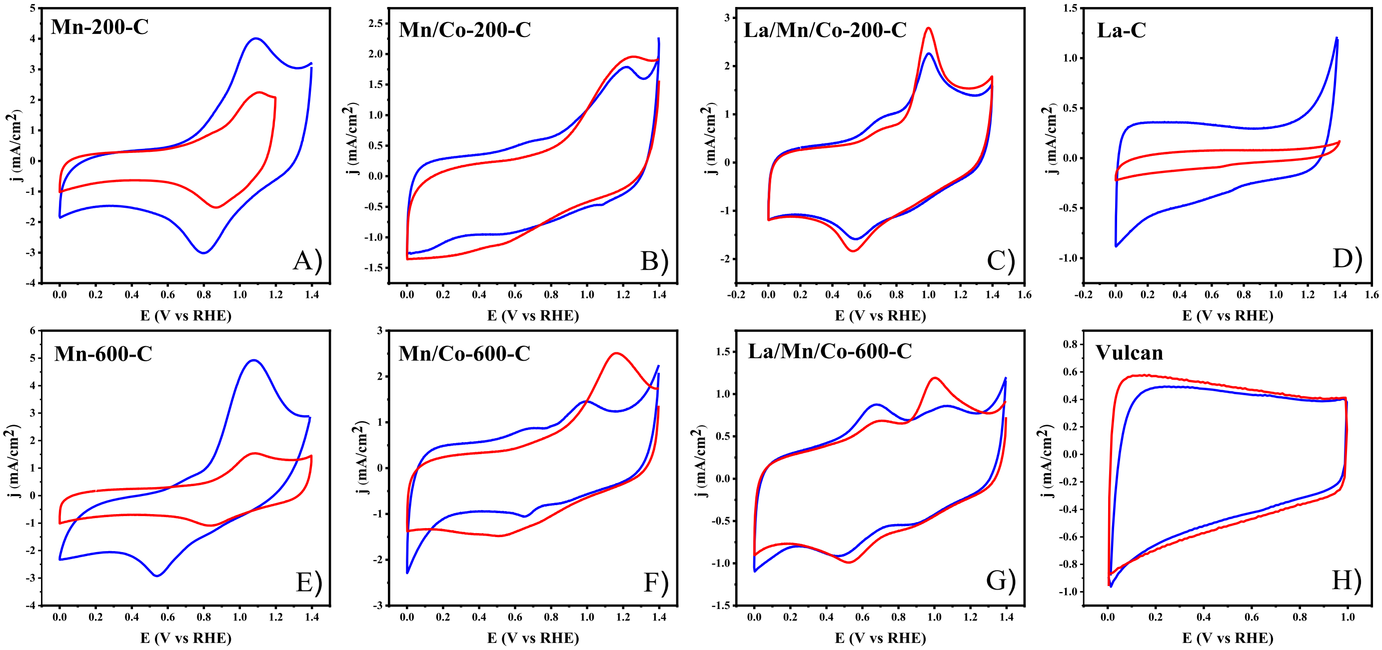

Fig. 8. Cyclic voltammograms before (blue) and after (red) ORR evaluation of the samples: A) Mn-200-C, B) Mn/Co-200-C, C) La/Mn/Co-200-C, D) La-C, E) Mn-600-C, F) Mn/Co-600-C, G) La/Mn/Co-600-C and H) Vulcan.0.1 M KOH, v= 50 mV/s.

to enhance the stability of the composite.

On the other hand, due to the potential hydrolysis of Si-O-X (X: Si, Al, B) bonds in silicate-based glassware cells at elevated pH and their consequent influence on electrocatalytic activity [58], the electrolyte after the 3-hour chronoamperometric stability experiment of the ORR has been analyzed using ICP-MS. The results (Table S1) reveal a negligible concentration of Si (much lower than the 35 ppm value mentioned in the literature [58]), Al, and B elements, indicating that they are not considered to impact electrocatalytic activity. Moreover, in Table S1, it can be observed that there is no considerable leaching of the metals composing the electrocatalyst: La, Mn, and Co, and Fe related to the KOH purity has not been detected. Moreover, the cyclic voltammetry of the commercial Pt/C electrocatalyst after the stability test shows the typical profile characteristic of this electrode (Fig. S12).

3.7. Rechargeable Zn-air battery tests

Rechargeable zinc-air batteries (ZABs) were assembled and tested at room temperature, using the battery depicted in Fig. S1. The air cathodes (positive electrodes) consisted of carbon paper (gas diffusion layer) loaded with three different materials: La/Mn/Co-200-C, Mn/Co-600-C, and the mixture of commercial Pt/C + RuO_2 catalysts. Fig. 9A presents the discharge polarization curves of the ZABs prepared with these three samples. The Mn/Co-600-C sample displayed superior performance over La/Mn/Co-200-C at low current densities due to a higher ohmic drop observed in the latter. However, both materials exhibited similar maximum power output (51.0 and 51.5 mW/cm^2, respectively). While the commercial Pt/C + RuO_2 catalyst demonstrated better electrocatalytic activity during the discharge process, neither of the synthesized materials in this work managed to surpass its activity in the discharge polarization curve.

Fig. 9B shows the galvanostatic discharge voltages at current densities ranging from 2 to 50 mA/cm^2 for ZABs prepared with La/Mn/Co-200-C and Mn/Co-600-C samples. The discharge voltages remained stable, which is crucial for practical applications [59], and the ZAB with La/Mn/Co-200-C exhibited higher voltages at high current densities. Interestingly, the discharge voltage could be restored to its initial value after reducing the current density in both samples, indicating excellent rate capability of the electrocatalysts.

Fig. 9C illustrates the discharge polarization curves at 5 and 10 mA/cm^2 for the ZAB containing La/Mn/Co-200-C, resulting in energy densities of 724 and 699 mAh/g, respectively. These values were higher than those obtained for the Mn/Co-600-C sample (Fig. S13).

The galvanostatic cycling test (Fig. 9D) was performed for La/Mn/Co-200-C and commercial Pt/C + RuO_2 catalyst at 1 mA/cm^2, with each charge-discharge cycle lasting 20 min. The La/Mn/Co-200-C sample exhibited long-term durability, operating under stable conditions for at least 120 h. Initially, the sample showed a charge and discharge voltage of 1.82 V and 1.32 V, respectively, resulting in an initial round-trip efficiency of 72.5 %. Commercial Pt/C + RuO_2 displayed a charge and discharge voltage of 2.06 V and 1.24 V, respectively, leading to an initial round-trip efficiency of 60.2 %. This demonstrates that the synthesized materials offer rechargeability for the target reactions and perform better than the commercial Pt/C + RuO_2 electrocatalyst. As the number of cycles increased, the efficiency decreased for both ZABs. However, after 249 charge-discharge cycles, the commercial Pt/C + RuO_2 catalyst loses its activity, concluding the experiment. Meanwhile, the La/Mn/Co-200-C sample continues to exhibit excellent performance for up to 360 cycles for 120 h, with a round-trip efficiency of 40.9 %.

When these results are compared with other studies from the literature using metal oxides as electrocatalysts in Zn-air batteries, it can be

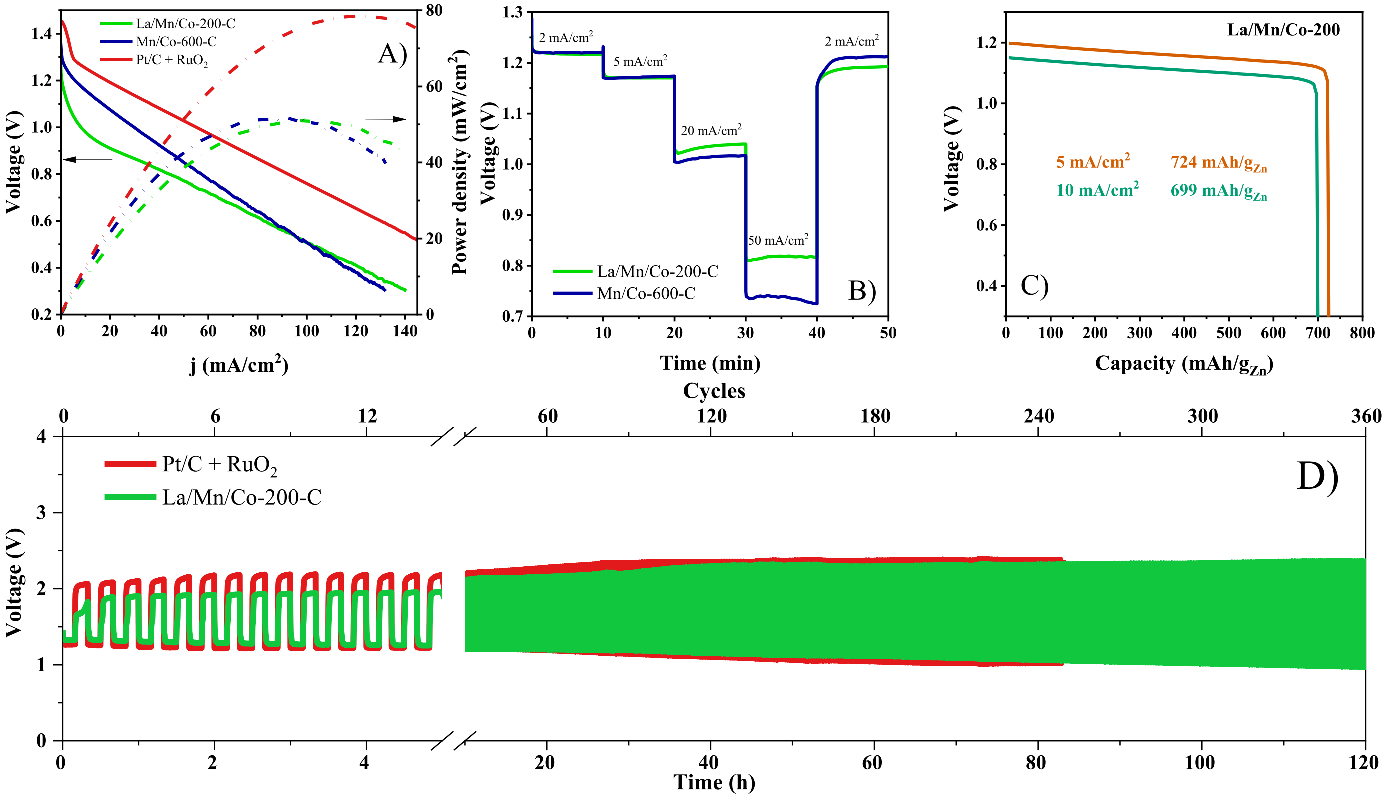

Fig. 9. A) Discharge polarization curves and corresponding power density plots for La/Mn/Co-200-C, Mn/Co-600-C and commercial Pt/C + RuO_2 samples, solid lines refer to voltage and dashed lines to power density. B) Discharge curves of the ZAB based on La/Mn/Co-200-C and Mn/Co-600-C with current densities from 2 to 50 mA/cm^2. C) Galvanostatic discharge curve at 5 mA/cm^2 and 10 mA/cm^2 for La/Mn/Co-200-C sample. D) Cycling performance at 1 mA/cm^2 of the La/Mn/Co-200-C-based ZAB and its comparison with commercial Pt/C + RuO_2-based ZAB.

observed that the La/Mn/Co-200-C sample exhibits a higher specific capacity value than the published works to date [2,60–62]. Furthermore, this sample shows similar electrochemical performance in charge-discharge experiments conducted under the same conditions, but it displays greater long-term stability [63,64]. It is important to highlight that this sample outperforms our previous work [24] in all aspects, where a high-temperature calcination process was required, significantly increasing the synthesis cost. Furthermore, the performance of the electrocatalyst synthesized in this study has been compared with relevant electrocatalysts of similar nature from the literature (Table S2). Competitive power peak parameters, capacity, and stability are observed in comparison to materials synthesized at higher temperatures. Thus, in this study, a cost-effective electrocatalyst with excellent performance and durability has been obtained. Moreover, in this work, the study corresponding to the Zn anode has not been performed but the Zn anode plays an essential role in deteriorating the overall performance of these batteries due to the formation of dendrites that can occur during plating and stripping processes. These dendrites often fracture from their roots, causing an irreversible loss of electronic contact [65].

4. Conclusions

In this work, electrocatalysts based on La stabilized low crystallinity metal (hydro-)oxides have been synthesized by hydrothermal synthesis and further heat treatment at low temperature (i.e., 200 °C). The electrocatalytic results of the materials obtained after mixing with carbon black demonstrates the usefulness of this process for the development of economical, stable, and eco-friendly bifunctional electrocatalysts for ORR and OER.

The electrocatalysts calcined at a low temperature exhibited superior bifunctional activities than those heated at 600 °C. Among them, the La/Mn/Co-200-C sample stands out, which shows an extraordinary bifunctional activity. We demonstrate the significance of having a substantial concentration of active sites in a material with a less organized structure, as opposed to one with higher crystallinity. In addition, the improved performance seems also to be related to the interaction between the manganese and cobalt ions and the empty f orbitals of lanthanum. The interaction of the metal (hydro-) oxide with the carbon material (M-O-C) is also enhanced by the presence of lanthanum in the low-temperature calcination sample (La/Mn/Co-200-C). This work opens the possibility of studying the stabilizing effect of other cations with empty f orbitals and how it affects the properties of electroactive cations.

Finally, these materials were evaluated in a real application, such the Zn-air battery, and they showed remarkable results. Furthermore, because no precious metals are used, the cost of the Zn-air battery using hydrothermal-synthesized materials and calcined at low temperatures, is significantly lower than that of Pt/C+ RuO_2 catalyst, highlighting its greater economic potential.

CRediT authorship contribution statement

M. García-Rodríguez: Writing – original draft, Methodology, Investigation, Formal analysis, Data curation. **D. Cazorla-Amorós:** Writing – review & editing, Supervision, Resources, Methodology, Investigation. **E. Morallón:** Writing – review & editing, Supervision, Resources, Methodology, Investigation, Funding acquisition, Conceptualization.

Declaration of competing interest

The authors declare that they have no known competing financial interests or personal relationships that could have appeared to influence the work reported in this paper.

Data availability

Data will be made available on request.

Acknowledgments

The authors would like to thank PID2019–105923RB-I00 and PID2022–137566OB-I00 projects funded by MCIN/AEI/10.13039/501100011033 and by “ERDF A way of making Europe”, by the “European Union”. M.G.R. thanks Ministerio de Universidades for the FPU20–01746 grant.

Supplementary materials

Supplementary material associated with this article can be found, in the online version, at doi:10.1016/j.electacta.2024.143858.

References

[1] M. Armand, J.M. Tarascon, Building better batteries, Nature 451 (2008) 652–657, https://doi.org/10.1038/451652a.

[2] Y. Li, M. Gong, Y. Liang, J. Feng, J.E. Kim, H. Wang, G. Hong, B. Zhang, H. Dai, Advanced zinc-air batteries based on high-performance hybrid electrocatalysts, Nat. Commun. 4 (2013) 1805, https://doi.org/10.1038/ncomms2812.

[3] D. Jiao, Z. Ma, J. Li, Y. Han, J. Mao, T. Ling, S. Qiao, Test factors affecting the performance of zinc–air battery, J. Energy Chem. 44 (2020) 1–7, https://doi.org/10.1016/j.jechem.2019.09.008.

[4] X. Hu, T. Yang, Z. Yang, Z. Li, R. Wang, M. Li, G. Huang, B. Jiang, C. Xu, F. Pan, Engineering of Co_3O_4@Ni_2P heterostructure as trifunctional electrocatalysts for rechargeable zinc-air battery and self-powered overall water splitting, J. Mater. Sci. Technol. 115 (2022) 19–28, https://doi.org/10.1016/j.jmst.2021.10.038.

[5] R. Wang, Z. Meng, X. Yan, T. Tian, M. Lei, R.A. Pashameah, H.M. Abo-Dief, H. Algadi, N. Huang, Z. Guo, H. Tang, Tellurium intervened Fe-N codoped carbon for improved oxygen reduction reaction and high-performance Zn-air batteries, J. Mater. Sci. Technol. 137 (2023) 215–222, https://doi.org/10.1016/j.jmst.2022.07.041.

[6] D. Papageorgopoulos, 2018 Merit Review and Peer Evaluation Meeting, Washington DC, 2018. https://www.hydrogen.energy.gov/annual-review/annual_review18_report.html.

[7] U. Martinez, S. Komini Babu, E.F. Holby, H.T. Chung, X. Yin, P. Zelenay, Progress in the development of Fe-based PGM-free electrocatalysts for the oxygen reduction reaction, Adv. Mater. 31 (2019) 1806545, https://doi.org/10.1002/adma.201806545.

[8] J. Pan, Y.Y. Xu, H. Yang, Z. Dong, H. Liu, B.Y. Xia, Advanced architectures and relatives of air electrodes in Zn-air batteries, Adv. Sci. 5 (2018) 1700691, https://doi.org/10.1002/advs.201700691.

[9] Y. Liang, Y. Li, H. Wang, J. Zhou, J. Wang, T. Regier, H. Dai, Co_3O_4 nanocrystals on graphene as a synergistic catalyst for oxygen reduction reaction, Nat. Mater. 10 (2011) 780–786, https://doi.org/10.1038/nmat3087.

[10] D.M. Morales, M.A. Kazakova, S. Dieckhöfer, A.G. Selyutin, G.V. Golubtsov, W. Schuhmann, J. Masa, Trimetallic Mn-Fe-Ni oxide nanoparticles supported on multi-walled carbon nanotubes as high-performance bifunctional ORR/OER electrocatalyst in alkaline media, Adv. Funct. Mater. 30 (2020) 1905992, https://doi.org/10.1002/adfm.201905992.

[11] D.A. Kuznetsov, B. Han, Y. Yu, R.R. Rao, J. Hwang, Y. Román-Leshkov, Y. Shao-Horn, Tuning redox transitions via inductive effect in metal oxides and complexes, and implications in oxygen electrocatalysis, Joule 2 (2018) 225–244, https://doi.org/10.1016/j.joule.2017.11.014.

[12] J.X. Flores-Lasluisa, F. Huerta, D. Cazorla-Amorós, E. Morallón, Transition metal oxides with perovskite and spinel structures for electrochemical energy production applications, Environ. Res. 214 (2022) 113731, https://doi.org/10.1016/j.envres.2022.113731.

[13] J. Suntivich, H.A. Gasteiger, N. Yabuuchi, H. Nakanishi, J.B. Goodenough, Y. Shao-Horn, Design principles for oxygen-reduction activity on perovskite oxide catalysts for fuel cells and metal–air batteries, Nat. Chem. 3 (2011) 546–550, https://doi.org/10.1038/nchem.1069.

[14] V. Celorrio, L. Calvillo, G. Granozzi, A.E. Russell, D.J. Fermin, $AMnO_3$ (A = Sr, La, Ca, Y) perovskite oxides as oxygen reduction electrocatalysts, Top. Catal. 61 (2018) 154–161, https://doi.org/10.1007/s11244-018-0886-5.

[15] Y. Wang, J. Li, Z. Wei, Transition-metal-oxide-based catalysts for the oxygen reduction reaction, J. Mater. Chem. A. 6 (2018) 8194–8209, https://doi.org/10.1039/C8TA01321G.

[16] Y. Wang, R. Gan, Z. Ai, H. Liu, C. Wei, Y. Song, M. Dirican, X. Zhang, C. Ma, J. Shi, Hollow Co_3O_{4-x} nanoparticles decorated N-doped porous carbon prepared by one-step pyrolysis as an efficient ORR electrocatalyst for rechargeable Zn-air batteries, Carbon N. Y. 181 (2021) 87–98, https://doi.org/10.1016/j.carbon.2021.05.016.

[17] K. Kumar, C. Canaff, J. Rousseau, S. Arrii-Clacens, T.W. Napporn, A. Habrioux, K. B. Kokoh, Effect of the oxide–carbon heterointerface on the activity of Co_3O_4/

NRGO nanocomposites toward ORR and OER, J. Phys. Chem. C. 120 (2016) 7949–7958, https://doi.org/10.1021/acs.jpcc.6b00313.

[18] A.S. Ryabova, A. Bonnefont, P.A. Simonov, T. Dintzer, C. Ulhaq-Bouillet, Y. G. Bogdanova, G.A. Tsirlina, E.R. Savinova, Further insights into the role of carbon in manganese oxide/carbon composites in the oxygen reduction reaction in alkaline media, Electrochim. Acta. 246 (2017) 643–653, https://doi.org/10.1016/j.electacta.2017.06.017.

[19] R.I. Walton, Perovskite oxides prepared by hydrothermal and solvothermal synthesis: a review of crystallisation, chemistry, and compositions, Chem. – A Eur. J. 26 (2020) 9041–9069, https://doi.org/10.1002/chem.202000707.

[20] M.R. Gao, J. Jiang, S.H. Yu, Solution-based synthesis and design of late transition metal chalcogenide materials for oxygen reduction reaction (ORR), Small 8 (2012) 13–27, https://doi.org/10.1002/smll.201101573.

[21] A. Muzaffar, M. Basheer Ahamed, K. Deshmukh, Hydrothermal synthesis of $ZnWO_4$–MnO_2 nanopowder doped with carbon black nanoparticles for high-performance supercapacitor applications, J. Mater. Sci. Mater. Electron. 30 (2019) 21250–21258, https://doi.org/10.1007/s10854-019-02498-0.

[22] T. Gupta, J.Cho Samriti, J. Prakash, Hydrothermal synthesis of TiO_2 nanorods: formation chemistry, growth mechanism, and tailoring of surface properties for photocatalytic activities, Mater. Today Chem. 20 (2021) 100428, https://doi.org/10.1016/j.mtchem.2021.100428.

[23] S. Zhao, Y. Shen, X. Yan, P. Zhou, Y. Yin, R. Lu, C. Han, B. Cui, D. Wei, Complex-surfactant-assisted hydrothermal synthesis of one-dimensional ZnO nanorods for high-performance ethanol gas sensor, Sensors Actuators B Chem 286 (2019) 501–511, https://doi.org/10.1016/j.snb.2019.01.127.

[24] M. García-Rodríguez, J.X. Flores-Lasluisa, D. Cazorla-Amorós, E. Morallón, Metal oxide Perovskite-Carbon composites as electrocatalysts for zinc-air batteries. Optimization of ball-milling mixing parameters, J. Colloid Interface Sci. 630 (2023) 269–280, https://doi.org/10.1016/j.jcis.2022.10.086.

[25] Y. Waseda, E. Matsubara, K. Shinoda, X-Ray Diffraction Crystallography, Springer Berlin Heidelberg, Berlin, Heidelberg, 2011, https://doi.org/10.1007/978-3-642-16635-8.

[26] A. Bard, L.R. Faulkner, Electrochemical Methods: Fundamentals and Applications, 2nd Editio, Wiley, 2001.

[27] J.X. Flores-Lasluisa, F. Huerta, D. Cazorla-Amorós, E. Morallón, Structural and morphological alterations induced by cobalt substitution in $LaMnO_3$ perovskites, J. Colloid Interface Sci. 556 (2019) 658–666, https://doi.org/10.1016/j.jcis.2019.08.112.

[28] Y. Li, D. Li, S. Fan, T. Yang, Q. Zhou, Facile template synthesis of dumbbell-like Mn_2O_3 with oxygen vacancies for efficient degradation of organic pollutants by activating peroxymonosulfate, Catal. Sci. Technol. 10 (2020) 864–875, https://doi.org/10.1039/C9CY01849B.

[29] J.P.H. Li, X. Zhou, Y. Pang, L. Zhu, E.I. Vovk, L. Cong, A.P. van Bavel, S. Li, Y. Yang, Understanding of binding energy calibration in XPS of lanthanum oxide by in situ treatment, Phys. Chem. Chem. Phys. 21 (2019) 22351–22358, https://doi.org/10.1039/C9CP04187G.

[30] C.K. Jørgensen, H. Berthou, Split photo-electron signals from the unique closed-shell cation lanthanum(III), Chem. Phys. Lett. 13 (1972) 186–189, https://doi.org/10.1016/0009-2614(72)85038-3.

[31] M.F. Sunding, K. Hadidi, S. Diplas, O.M. Løvvik, T.E. Norby, A.E. Gunnæs, XPS characterisation of in situ treated lanthanum oxide and hydroxide using tailored charge referencing and peak fitting procedures, J. Electron Spectros. Relat. Phenomena. 184 (2011) 399–409, https://doi.org/10.1016/j.elspec.2011.04.002.

[32] H. Wang, M. Zhou, P. Choudhury, H. Luo, Perovskite oxides as bifunctional oxygen electrocatalysts for oxygen evolution/reduction reactions – a mini review, Appl. Mater. Today. 16 (2019) 56–71, https://doi.org/10.1016/j.apmt.2019.05.004.

[33] J. Liu, X. Jin, W. Song, F. Wang, N. Wang, Y. Song, Facile preparation of modified carbon black-$LaMnO_3$ hybrids and the effect of covalent coupling on the catalytic activity for oxygen reduction reaction, Chin. J. Catal. 35 (2014) 1173–1188, https://doi.org/10.1016/S1872-2067(14)60066-8.

[34] W. Chen, C. Xia, H.N. Alshareef, One-step electrodeposited nickel cobalt sulfide nanosheet arrays for high-performance asymmetric supercapacitors, ACS Nano 8 (2014) 9531–9541, https://doi.org/10.1021/nn503814y.

[35] J.X. Flores-Lasluisa, F. Huerta, D. Cazorla-Amorós, E. Morallon, Carbon material and cobalt-substitution effects in the electrochemical behavior of $LaMnO_3$ for ORR and OER, Nanomaterials 10 (2020) 2394, https://doi.org/10.3390/nano10122394.

[36] Y. Zhu, W. Zhou, Z. Shao, Perovskite/carbon composites: applications in oxygen electrocatalysis, Small 13 (2017) 1603793, https://doi.org/10.1002/smll.201603793.

[37] J.A. Haber, N.S. Lewis, Infrared and X-ray photoelectron spectroscopic studies of the reactions of hydrogen-terminated crystalline Si(111) and Si(100) surfaces with Br_2, I_2, and ferrocenium in alcohol solvents, J. Phys. Chem. B. 106 (2002) 3639–3656, https://doi.org/10.1021/jp0102872.

[38] Y. Okamoto, H. Nakano, T. Imanaka, S. Teranishi, X-ray photoelectron spectroscopic studies of catalysts — supported cobalt catalysts —, Bull. Chem. Soc. Jpn. 48 (1975) 1163–1168, https://doi.org/10.1246/bcsj.48.1163.

[39] J. Huang, Y. Jiang, M. Hunger, Influence of the lanthanum exchange degree on the concentration and acid strength of bridging hydroxyl groups in zeolites La, Na-X (2007) 622–628, https://doi.org/10.1016/S0167-2991(07)80900-1, inpp.

[40] E.R. Stobbe, B.A. de Boer, J.W. Geus, The reduction and oxidation behaviour of manganese oxides, Catal. Today. 47 (1999) 161–167, https://doi.org/10.1016/S0920-5861(98)00296-X.

[41] O.A. Bulavchenko, E.Y. Gerasimov, T.N. Afonasenko, Reduction of double manganese–cobalt oxides: in situ XRD and TPR study, Dalt. Trans. 47 (2018) 17153–17159, https://doi.org/10.1039/C8DT04137G.

[42] L. Meng, J. Wang, Z. Sun, J. Zhu, H. Li, J. Wang, M. Shen, Active manganese oxide on MnO_x–CeO_2 catalysts for low-temperature NO oxidation: characterization and kinetics study, J. Rare Earths. 36 (2018) 142–147, https://doi.org/10.1016/j.jre.2017.05.017.

[43] L.J. Garces, B. Hincapie, R. Zerger, S.L. Suib, The effect of temperature and support on the reduction of cobalt oxide: an in situ X-ray diffraction study, J. Phys. Chem. C. 119 (2015) 5484–5490, https://doi.org/10.1021/jp5124184.

[44] A. Ul R. Salman, S.M. Hyrve, S.K. Regli, M. Zubair, B.C. Enger, R. Lødeng, D. Waller, M. Rønning, Catalytic oxidation of NO over $LaCo_{1-x}B_xO_3$ (B = Mn, Ni) perovskites for nitric acid production, Catalysts 9 (2019) 429, https://doi.org/10.3390/catal9050429.

[45] H. Liu, X. Zhu, M. Li, Q. Tang, G. Sun, W. Yang, Single crystal $(Mn,Co)_3O_4$ octahedra for highly efficient oxygen reduction reactions, Electrochim. Acta. 144 (2014) 31–41, https://doi.org/10.1016/j.electacta.2014.08.087.

[46] Z. Wang, W.A. Perera, S. Perananthan, J.P. Ferraris, K.J. Balkus, Lanthanum hydroxide nanorod-templated graphitic hollow carbon nanorods for supercapacitors, ACS Omega 3 (2018) 13913–13918, https://doi.org/10.1021/acsomega.8b01714.

[47] W. Wang, E. Liu, Y. Hu, L. Jiao, P. Kolla, Y. Liu, M. Tang, J. Luo, Q. Sun, S. Chen, Q. Jia, S. Mukerjee, Understanding the ORR electrocatalysis on Co–Mn oxides, J. Phys. Chem. C. 125 (2021) 25470–25477, https://doi.org/10.1021/acs.jpcc.1c00104.

[48] A.S. Ryabova, F.S. Napolskiy, T. Poux, S.Y. Istomin, A. Bonnefont, D.M. Antipin, A. Y. Baranchikov, E.E. Levin, A.M. Abakumov, G. Kéranguéven, E.V. Antipov, G. A. Tsirlina, E.R. Savinova, Rationalizing the influence of the Mn(IV)/Mn(III) Red-Ox transition on the electrocatalytic activity of manganese oxides in the oxygen reduction reaction, Electrochim. Acta. 187 (2016) 161–172, https://doi.org/10.1016/j.electacta.2015.11.012.

[49] C. Zhu, D. Wen, S. Leubner, M. Oschatz, W. Liu, M. Holzschuh, F. Simon, S. Kaskel, A. Eychmüller, Nickel cobalt oxide hollow nanosponges as advanced electrocatalysts for the oxygen evolution reaction, Chem. Commun. 51 (2015) 7851–7854, https://doi.org/10.1039/C5CC01558H.

[50] G. Alemany-Molina, J. Quílez-Bermejo, M. Navlani-García, E. Morallón, D. Cazorla-Amorós, Efficient and cost-effective ORR electrocatalysts based on low content transition metals highly dispersed on C_3N_4/super-activated carbon composites, Carbon N. Y. 196 (2022) 378–390, https://doi.org/10.1016/j.carbon.2022.05.003.

[51] J.H. Zagal, M.T.M. Koper, Reactivity descriptors for the activity of molecular MN4 catalysts for the oxygen reduction reaction, Angew. Chemie Int. Ed. 55 (2016) 14510–14521, https://doi.org/10.1002/anie.201604311.

[52] C. Zúñiga, C. Candia-Onfray, R. Venegas, K. Muñoz, J. Urra, M. Sánchez-Arenillas, J.F. Marco, J.H. Zagal, F.J. Recio, Elucidating the mechanism of the oxygen reduction reaction for pyrolyzed Fe-N-C catalysts in basic media, Electrochem. Commun. 102 (2019) 78–82, https://doi.org/10.1016/j.elecom.2019.04.005.

[53] M. Schalenbach, O. Kasian, M. Ledendecker, F.D. Speck, A.M. Mingers, K.J. J. Mayrhofer, S. Cherevko, The electrochemical dissolution of noble metals in alkaline media, Electrocatalysis 9 (2018) 153–161, https://doi.org/10.1007/s12678-017-0438-y.

[54] O. Galindev, T. Takeguchi, M.M. Rahman, Understanding the mechanisms and design principles for oxygen evolution and oxygen reduction activity on perovskite catalysts for alkaline zinc–air batteries, Catal. Sci. Technol. 11 (2021) 5200–5211, https://doi.org/10.1039/D1CY00657F.

[55] M. Akbayrak, A.M. Önal, Metal oxides supported cobalt nanoparticles: active electrocatalysts for oxygen evolution reaction, Electrochim. Acta. 393 (2021) 139053, https://doi.org/10.1016/j.electacta.2021.139053.

[56] T. Shinagawa, A.T. Garcia-Esparza, K. Takanabe, Insight on Tafel slopes from a microkinetic analysis of aqueous electrocatalysis for energy conversion, Sci. Rep. 5 (2015) 13801, https://doi.org/10.1038/srep13801.

[57] N. Fujiwara, T. Nagai, T. Ioroi, H. Arai, Z. Ogumi, Bifunctional electrocatalysts of lanthanum-based perovskite oxide with Sb-doped SnO_2 for oxygen reduction and evolution reactions, J. Power Sources. 451 (2020) 227736, https://doi.org/10.1016/j.jpowsour.2020.227736.

[58] K.J.J. Mayrhofer, A.S. Crampton, G.K.H. Wiberg, M. Arenz, Analysis of the impact of individual glass constituents on electrocatalysis on pt electrodes in alkaline solution, J. Electrochem. Soc. 155 (2008) P78, https://doi.org/10.1149/1.2904882.

[59] N. Li, L. Li, J. Xia, M. Arif, S. Zhou, F. Yin, G. He, H. Chen, Single-atom Co-N_4 catalytic sites anchored on N-doped ordered mesoporous carbon for excellent Zn-air batteries, J. Mater. Sci. Technol. 139 (2023) 224–231, https://doi.org/10.1016/j.jmst.2022.07.058.

[60] M. Prabu, K. Ketpang, S. Shanmugam, Hierarchical nanostructured $NiCo_2O_4$ as an efficient bifunctional non-precious metal catalyst for rechargeable zinc–air batteries, Nanoscale 6 (2014) 3173, https://doi.org/10.1039/c3nr05835b.

[61] S. Chen, S. Chen, J. Zhang, Thermal sugar bubbling preparation of N-doped porous carbon for high-performance solid-state Zn-air batteries, Batter. Supercaps. 2 (2019) 373–379, https://doi.org/10.1002/batt.201800105.

[62] X. Liu, M. Park, M.G. Kim, S. Gupta, G. Wu, J. Cho, Integrating NiCo alloys with their oxides as efficient bifunctional cathode catalysts for rechargeable zinc-air batteries, Angew. Chemie Int. Ed. 54 (2015) 9654–9658, https://doi.org/10.1002/anie.201503612.

[63] L. Zhang, Y. Zhu, Z. Nie, Z. Li, Y. Ye, L. Li, J. Hong, Z. Bi, Y. Zhou, G. Hu, Co/MoC nanoparticles embedded in carbon nanoboxes as robust trifunctional

electrocatalysts for a Zn–air battery and water electrocatalysis, ACS Nano 15 (2021) 13399–13414, https://doi.org/10.1021/acsnano.1c03766.

[64] J. Yin, J. Jin, H. Liu, B. Huang, M. Lu, J. Li, H. Liu, H. Zhang, Y. Peng, P. Xi, C. Yan, $NiCo_2O_4$-based nanosheets with uniform 4nm mesopores for excellent Zn–Air battery performance, Adv. Mater. 32 (2020), https://doi.org/10.1002/adma.202001651.

[65] Y. Yang, H. Yang, R. Zhu, H. Zhou, High reversibility at high current density: the zinc electrodeposition principle behind the "trick, Energy Environ. Sci. 16 (2023) 2723–2731, https://doi.org/10.1039/D3EE00925D.